




# Nonlinear Alfvén Wave Model of Stellar Coronae and Winds from the Sun to M Dwarfs

Takahito Sakaue  and Kazunari Shibata

Astronomical Observatory, Kyoto University, Japan; [sakaue@kwasan.kyoto-u.ac.jp](mailto:sakaue@kwasan.kyoto-u.ac.jp)

Received 2020 November 20; revised 2020 December 14; accepted 2020 December 14; published 2021 January 13

## Abstract

An M dwarf’s atmosphere and wind are expected to be highly magnetized. The nonlinear propagation of Alfvén waves could play a key role in both heating the stellar atmosphere and driving the stellar wind. Using this Alfvén wave scenario, we carried out a one-dimensional compressive magnetohydrodynamic simulation to examine the nonlinear propagation of Alfvén waves from the M dwarf’s photosphere, chromosphere to the corona, and interplanetary space. Based on the simulation results, we developed a semi-empirical method describing the solar and M dwarf’s coronal temperature, stellar wind velocity, and wind’s mass-loss rate. We find that M dwarfs’ coronae tend to be cooler than the solar corona, and that M dwarfs’ stellar winds can be characterized as having a faster velocity and much smaller mass-loss rate compared to those of the solar wind.

*Unified Astronomy Thesaurus concepts:* [Stellar winds \(1636\)](#); [Stellar coronae \(305\)](#); [Stellar chromospheres \(230\)](#); [M dwarf stars \(982\)](#); [Alfvén waves \(23\)](#); [Magnetohydrodynamics \(1964\)](#)

## 1. Introduction

M-type main-sequence stars (M dwarfs) have a highly magnetized atmosphere. Discussion of their magnetic activities has focused in particular on their impact on the planetary atmosphere (Khodachenko et al. 2007; Lammer et al. 2007; Scalo et al. 2007; Tarter et al. 2007; Seager 2013). It is important for studies about exoplanets or astrobiology to reveal the underlying physics for the structure of the stellar atmosphere and wind (Vidotto et al. 2014; Linsky 2019; Mesquita & Vidotto 2020).

The most promising mechanism for both heating the stellar atmosphere and driving the stellar wind is the nonlinear processes related to Alfvén waves (Velli 1993; Cranmer & Saar 2011). Alfvén waves are responsible for the transfer of magnetic energy in the magnetized plasma, and are involved in energy conversion to kinetic or thermal energy of the background media through nonlinear processes. Based on this scenario, the three-dimensional (3D) magnetohydrodynamic (MHD) global model for the solar atmosphere and wind (Alfvén Wave Solar Model (AWSOM) by van der Holst et al. 2014) has been developed to investigate the stellar wind of M dwarfs and the environments around their planets (Cohen et al. 2014; Garraffo et al. 2017; Dong et al. 2018; Alvarado-Gómez et al. 2020).

Although these studies discuss the 3D global structure of the stellar wind and magnetic field configuration, their applicability is limited due to the following two properties intrinsic to their models. First, the inner boundary of their models is placed at the “top of the stellar chromosphere,” and the Alfvén wave amplitude on that height is given by the empirical law (Sokolov et al. 2013). Second, the interaction between the Alfvén wave and the stellar wind is considered in a much simplified way using analytical, empirical, or phenomenological terms, because the propagating Alfvén wave cannot be resolved directly in the 3D simulations owing to the low spatial resolution. The effect of the other compressible waves on the stellar wind and Alfvén wave propagation is neglected.

These difficulties in the above 3D global model have been addressed by numerical studies about the nonlinear propagation of Alfvén waves along the single magnetic flux tube in the solar atmosphere from the photosphere and chromosphere to the corona (Hollweg et al. 1982; Kudoh & Shibata 1999;

Matsumoto & Shibata 2010) and solar wind (Suzuki & Inutsuka 2005, 2006; Matsumoto & Suzuki 2012, 2014; Shoda et al. 2018, 2019; Matsumoto 2021; Sakaue & Shibata 2020). These approaches also have been extended to the stellar atmosphere and wind models (Suzuki et al. 2013; Suzuki 2018; Shoda et al. 2020), and have revealed that the Alfvén wave amplitude on the top of chromosphere should be self-consistently determined as a consequence of wave dissipation and reflection in the chromosphere. In addition, owing to their high-resolution simulations, it is found that, while the atmosphere and wind are maintained by the energy and momentum transfer by Alfvén waves, its propagation is affected by the dynamics of atmosphere and wind. These studies highlight the importance of resolving the local dynamics associated with Alfvén wave propagation, as well as reproducing the global structure of the solar and stellar atmosphere and wind.

In this Letter, we extend our recent solar atmosphere and wind model (Sakaue & Shibata 2020) to the M dwarf’s atmosphere and wind. By carrying out one-dimensional (1D) time-dependent MHD simulations, the nonlinear propagation of Alfvén waves in the nonsteady stellar atmosphere and wind is calculated from the M dwarf’s photosphere and chromosphere to the corona and interplanetary space. The primary goal of this Letter is to summarize the differences in the reproduced stellar atmosphere and wind structures between the Sun and M dwarfs. The physical mechanisms for such a diversity of stellar atmospheres and wind are also discussed here and will be more quantitatively investigated in a subsequent paper (Sakaue & Shibata 2021, in preparation), in which we develop the semi-empirical method describing the stellar atmosphere and wind parameters (coronal temperature, wind velocity and mass-loss rate) based on the simulation results.

## 2. Numerical Setting

The nonlinear propagation of the Alfvén wave in the time-dependent stellar atmosphere and wind is simulated by using 1D MHD equations based on the axial symmetry assumption of the magnetic flux tube (see Appendix A and Sakaue & Shibata 2020). The surface of the axisymmetric flux tube is defined by the poloidal and toroidal axes, which are noted in this study with  $x$  and  $\phi$  (Figure 1). There are three free parameters determining the

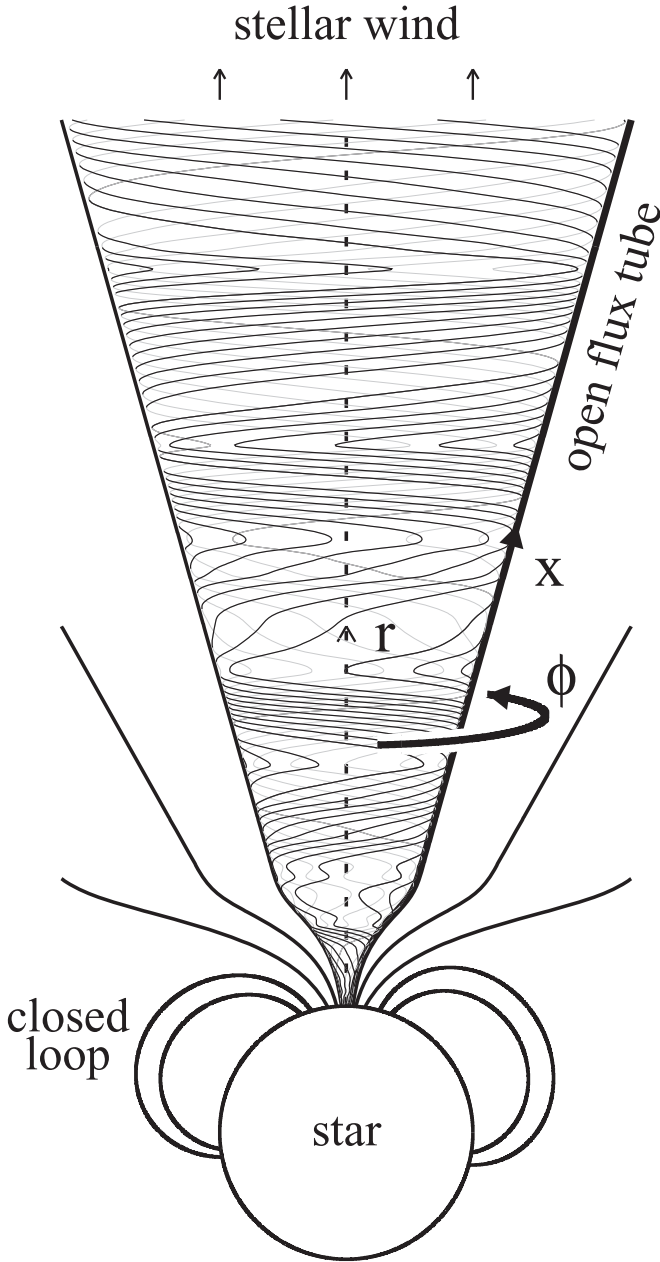


**Figure 1.** Schematic image of axisymmetric magnetic flux tube, the surface of which is defined by the poloidal  $x$  and toroidal  $\phi$  axes. The winding thin lines represent the magnetic field lines, which illustrate the nonlinear propagation of the Alfvén wave.

magnetic flux tube configuration used in this study, including the photospheric magnetic field strength ( $B_{ph}$ ), chromospheric magnetic field strength ( $\bar{B}$ ), and filling factor of the open flux tube on the photosphere ( $f_{ph}$ ). Among them,  $B_{ph}$  is assumed to be equipartition to the photospheric plasma pressure, and  $f_{ph}$  is fixed at  $1/1600$ .

By employing the different stellar photospheres as the boundary conditions, we considered the stellar atmospheres and winds of the Sun and two M dwarfs, AD Leo (M3.5) and TRAPPIST-1 (M8). The stellar mass ( $M_*$ ), radius ( $r_*$ ), and effective temperature ( $T_{eff}$ ) of AD Leo are  $0.47 M_\odot$ ,  $0.46 r_\odot$ , and  $3473$  K, respectively (Maldonado et al. 2015), where  $M_\odot = 2.0 \times 10^{33}$  g and  $r_\odot = 7.0 \times 10^{10}$  cm are the solar mass and radius. TRAPPIST-1's  $M_*$ ,  $r_*$ , and  $T_{eff}$  are  $0.08 M_\odot$ ,  $0.12 r_*$ , and  $2559$  K, respectively (Gillon et al. 2016). These basic parameters imply that M dwarfs are

characterized with the larger gravitational acceleration ( $g_*$ ), shorter pressure scale height of the photosphere ( $H_{ph} = RT_{eff}/(\mu_{ph}g_*)$ ), and almost the same surface escape velocity  $v_{esc*}$  compared to the Sun. In fact,  $\log_{10} g_* = 4.44, 4.79$ , and  $5.21$  for the Sun, AD Leo, and TRAPPIST-1, respectively.  $H_{ph} = 130, 29$ , and  $6.9$  km as well, and  $v_{esc*} = 618, 624$ , and  $511$  km s $^{-1}$ .

The outwardly propagating Alfvén wave is excited on the photosphere by imposing the velocity and magnetic fluctuations on the bottom boundary, which represent the surface convective motion. The mass density and convective velocity on the photosphere is calculated based on the opacity table presented by Freedman et al. (2014) and surface convection theory by Ludwig et al. (1999, 2002), and Magic et al. (2015). The outer boundary is set at  $r \gtrsim 100 r_*$ , and 19200 grids are placed nonuniformly. The numerical scheme is based on the HLLD Riemann solver (Miyoshi & Kusano 2005) with the second-order MUSCL interpolation and the third-order TVD Runge–Kutta method (Shu & Osher 1988). The heat conduction is solved by the super-time-stepping method (Meyer et al. 2012). We also performed the parameter survey about the chromospheric magnetic field strength and the velocity amplitude on the photosphere for each star.

### 3. Typical Simulation Results

After several tens of hours, the stellar wind in the simulation box reaches the quasi-steady state. In the particular case of the M3.5 dwarf shown in Figure 2, it is found that the stellar wind velocity reaches around  $900$  km s $^{-1}$ , and that the transition layer appears in the temperature profile around  $1$  Mm, dividing the lower-temperature chromosphere and  $1$  MK corona.

To characterize the physical quantities of quasi-steady state of stellar atmospheres and winds, we investigate the integrals of the basic equations. First is the integral of the equation of motion, which is obtained by temporally averaging and spatially integrating Equation (A3).

$$v_x^2(r) = \Delta_p^r + \Delta_{p_B}^r + \Delta_c^r + \Delta_t^r + \Delta_g^r. \quad (1)$$

The right-hand side terms are defined as  $\Delta_p^r = -2 \int_{r_*}^r \langle \frac{1}{\rho} \frac{\partial p}{\partial x} \rangle dx$ , where  $\langle \cdot \rangle$  means the temporal average,  $\Delta_{p_B}^r = -2 \int_{r_*}^r \langle \frac{1}{\rho} \frac{\partial}{\partial x} \left( \frac{B_\phi^2}{8\pi} \right) \rangle dx$ ,  $\Delta_c^r = 2 \int_{r_*}^r \langle v_\phi^2 \rangle \frac{\partial \ln \sqrt{A}}{\partial x} dx$ ,  $\Delta_t^r = -2 \int_{r_*}^r \langle \frac{B_\phi^2}{4\pi\rho} \rangle \frac{\partial \ln \sqrt{A}}{\partial x} dx$ , and  $\Delta_g^r = -v_{esc*}^2 \left( 1 - \frac{r_*}{r} \right)$ , where  $v_{esc*} = \sqrt{2GM_*/r_*}$  is the escape velocity on the stellar surface.

Another integral of equation describes the energy flux conservation.

$$A(F_A + F(v_x) + F_g + F_c + F_{rad}) = L_{total} = \text{const.} \quad (2)$$

where  $F_A = -B_x \langle B_\phi v_\phi \rangle / (4\pi)$  is Poynting flux by the magnetic tension (Alfvén wave energy flux),  $F_g = -\langle \rho v_x \rangle GM_*/r$  is the gravitational energy flux, and  $F_{rad} = \frac{1}{A} \int_{r_*}^r A \langle Q_{rad} \rangle dx'$  is the energy flux representing the radiative energy loss.  $F(v_x)$  is the sum of enthalpy flux  $F_{ent}$ , kinetic energy flux  $F_{kin}$ , and the Poynting flux advected by the stellar wind:  $F_{ent} = \gamma \langle p v_x \rangle / (\gamma - 1)$ ,  $F_{kin} = \langle \rho v^2 v_x \rangle / 2$ , and  $F(v_x) = F_{ent} + F_{kin} + \langle B_\phi^2 v_x \rangle / (4\pi)$ .

Equations (1) and (2) are confirmed in Figures 3(a) and (b), which show the simulation result of stellar wind for the M3.5 dwarf. In Figure 3(a), the black solid line corresponds to  $\Delta_p^r + \Delta_{p_B}^r + \Delta_t^r + \Delta_c^r$ , which agrees well with  $v_x^2$

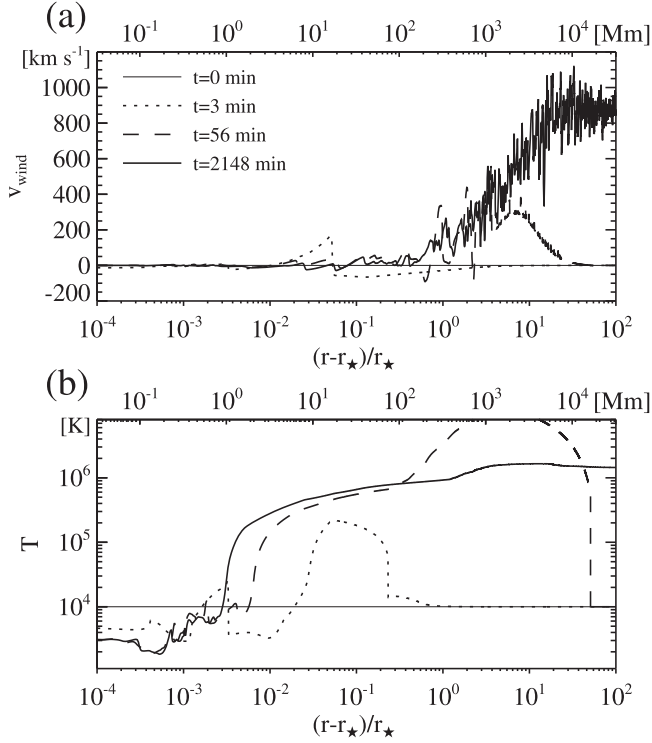


**Figure 2.** Temporal variations of the stellar wind velocity (panel (a)) and temperature (panel (b)) in the case of M3.5 dwarf ( $r_* = 0.46r_\odot$ ). The stellar wind velocity reaches around  $900 \text{ km s}^{-1}$ . The transition layer appears in the temperature profile, dividing the lower-temperature chromosphere and 10 MK corona.

(thick gray line) as indicated by Equation (1). It is most remarkable in Figure 3(a) that the stellar wind is mainly driven by the plasma pressure gradient (red solid line). In particular, the slow shocks excited by the nonlinear process of Alfvén waves greatly contribute to this stellar wind acceleration, which will be explained in Sakaue & Shibata (2021, in preparation) in more detail. The magnetic pressure gradient (green line) contributes to supporting the stellar atmosphere and driving the stellar wind within  $r \lesssim 10r_*$ , but not involved in the further acceleration of stellar wind beyond the distance where the Alfvén wave amplitude (orange line) reaches a maximum. The magnetic tension force decelerates the stellar wind against the acceleration by the centrifugal force (blue line). In Figure 3(b), the energy fluxes are normalized by  $F_{\text{mass}}GM_*/r_*$ , where  $F_{\text{mass}}$  is the mass flux and  $F_{\text{mass}}GM_*/r_* \approx 5 \times 10^3 r_*^2/(fr^2) \text{ erg cm}^{-2} \text{ s}^{-1}$ . It is confirmed that  $F_A$ ,  $F_g$ , and  $F_c$  determine the energy balance at the coronal height  $r - r_* \sim 0.1r_*$ , while in the distance ( $\gtrsim 10r_*$ ), the kinetic energy flux of the stellar wind ( $F_{\text{kin}}$ ) dominates the total energy flux. By defining  $L_{A,\text{co}}$ ,  $L_{g,\text{co}}$ ,  $L_{c,\text{co}}$  as the energy luminosities  $F_A A$ ,  $F_g A$ ,  $F_c A$  at  $r = 1.1r_*$  and  $L_{\text{kin},\text{wind}}$  as  $F_{\text{kin}} A$  at  $r = 100r_*$ , the energy conservation along the magnetic flux tube is approximately expressed as

$$L_{A,\text{co}} \approx L_{\text{kin},\text{wind}} - L_{g,\text{co}} - L_{c,\text{co}}. \quad (3)$$

The subscript  $\text{co}$  represents the physical quantities at  $r = r_{\text{co}} = 1.1r_*$ . The above relation shows that the Alfvén wave energy flux is converted to the wind’s energy loss  $L_{\text{kin},\text{wind}} - L_{g,\text{co}}$  and the coronal heating loss  $-L_{c,\text{co}}$ . Note that  $L_{\text{kin},\text{wind}} - L_{g,\text{co}} = \dot{M}(v_{\text{wind}}^2 + v_{\text{esc},*}^2)/2$ , where  $v_{\text{wind}} = v_x(r = 100r_*)$  is the wind velocity and  $\dot{M} = \rho v_x A$  is the mass-loss rate.

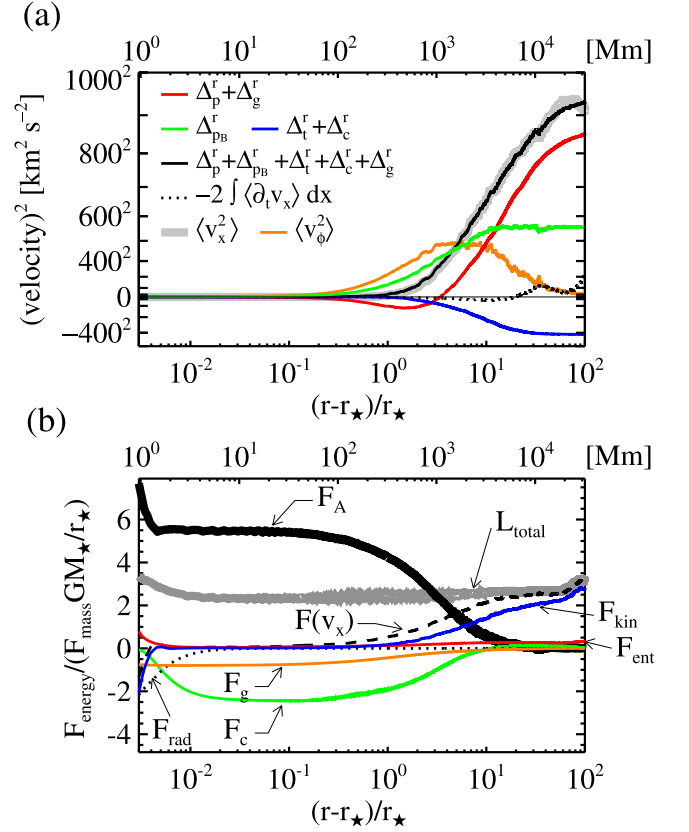


**Figure 3.** Momentum and energy conservations in the stellar wind of the M3.5 dwarf. In panel (a), the profile of  $v_x^2$  (thick gray line) is compared to the contributions by magnetic pressure acceleration  $\Delta_{PB}^r$  (green line), sum of plasma pressure  $\Delta_p^r$ , and gravitational acceleration  $\Delta_g^r$  (red line), and sum of centrifugal force  $\Delta_c^r$  and magnetic tension force  $\Delta_t^r$ . The orange line shows the profile of the square amplitude of the Alfvén wave. Panel (b) shows the energy fluxes normalized by  $F_{\text{mass}}GM_*/r_*$ , where  $F_{\text{mass}}$  is the mass flux and  $F_{\text{mass}}GM_*/r_* \approx 5 \times 10^3 r_*^2/(fr^2) \text{ erg cm}^{-2} \text{ s}^{-1}$ .  $F_A$ ,  $F_{\text{kin}}$ ,  $F_{\text{ent}}$ ,  $F_g$ ,  $F_{\text{rad}}$ ,  $F_c$ , and  $F(v_x)$  are Alfvén wave energy flux, kinetic energy flux, enthalpy flux, gravitational energy flux, heat conduction flux, and the sum of enthalpy flux, kinetic energy flux, and Poynting flux advected with the stellar wind, respectively.  $L_{\text{total}}$  is the integral constant in Equation (2).

#### 4. Stellar Coronae and Winds from the Sun to M Dwarfs

Numerical parameter surveys about the Sun and M dwarfs reveal the diversity of stellar wind velocity ( $v_{\text{wind}}$ ) and coronal temperature ( $T_{\text{co}}$ ). Figure 4 illustrates the general trends of such characteristics of stellar atmospheres and winds. In Figure 4(a),  $v_{\text{wind}}$  are plotted as a function of the maximum amplitude of Alfvén wave in the stellar wind ( $v_{\phi \text{ max}}$ ). The tight correlation between them is accounted for, because  $v_{\phi \text{ max}}$  well represents the strength of slow shocks that drive the stellar winds. The Alfvén wave tends to be more amplified in the stellar wind when  $T_{\text{co}}$  is cooler (Figure 4(b)). Figure 4(c) shows that  $T_{\text{co}}$  increases with the transmitted Poynting flux into the corona ( $F_{A,\text{co}}$ ), but M dwarfs’  $T_{\text{co}}$  are systematically cooler than that of the Sun for a given  $F_{A,\text{co}}$ . Finally, it is confirmed that the wind’s mass-loss rates ( $\dot{M}$ ) are well correlated with the energy luminosity of the Alfvén wave ( $L_{A,\text{co}}$ ), as shown in Figure 4(d).

#### 5. Semi-empirical Method to Predict the Characteristics of Stellar Atmosphere and Wind

In order to comprehend the physical mechanisms causing the relationships presented in Figure 4, we developed a semi-



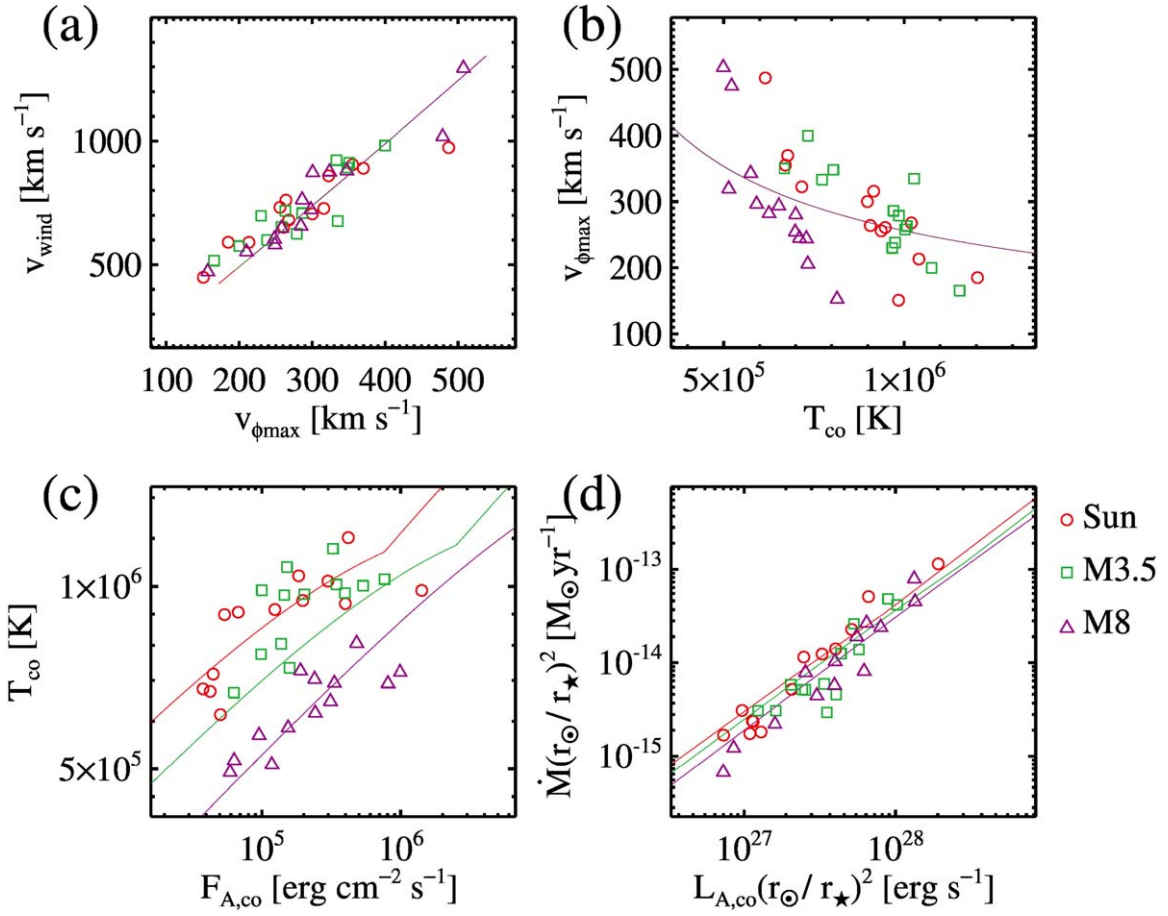


**Figure 4.** Characteristics of stellar atmospheres and winds obtained from the numerical parameter survey. The symbols represent the simulation results. The parameter survey for each star is carried out for the velocity amplitude on the photosphere (within  $(0.04\text{--}0.6) \times$  adiabatic sound speeds on the photosphere) and the chromospheric magnetic field strength (within  $(0.002\text{--}0.05) \times$  photospheric magnetic field strengths). The solid lines correspond to the prediction curves of our semi-empirical method. Panel (a): stellar wind velocity ( $v_{\text{wind}}$ ) vs. the maximum amplitude of the Alfvén wave in the stellar wind ( $v_{\phi \text{ max}}$ ). Panel (b):  $v_{\phi \text{ max}}$  vs. the coronal temperature ( $T_{\text{co}}$ ). Panel (c):  $T_{\text{co}}$  vs. the transmitted Poynting flux into the corona ( $F_{\text{A,co}}$ ). Panel (d): Alfvén wave luminosity in the corona ( $L_{\text{A,co}}$ ) vs. stellar wind’s mass-loss rate ( $\dot{M}$ ).

empirical method to calculate  $v_{\text{wind}}$ ,  $v_{\phi \text{ max}}$ , and  $T_{\text{co}}$  as functions of given effective temperature ( $T_{\text{eff}}$ ) and Alfvén wave luminosity on the stellar photosphere ( $L_{\text{A,ph}}$ ). Their derivation is briefly summarized in Appendix B and will be described in Sakaue & Shibata (2021, in preparation). The solid lines in Figure 4 are the prediction curves of our semi-empirical method. As shown in Figure 4, the positive or negative correlations among the physical quantities are correctly reproduced by our method, although the simulation results remain scattered around the prediction curves within a factor of  $\sim 2$ . This means that the following scenario, which is employed in our semi-empirical method, can account for the relationships shown in Figure 4, in both a qualitative and somewhat quantitative manner.

According to our semi-empirical method, the thinner atmosphere of the M dwarf is characterized by an increase in the temperature gradient in the corona ( $(\text{grad } T)_{\text{co}}$ ) for a given  $T_{\text{co}}$ . The larger  $(\text{grad } T)_{\text{co}}$ , the cooler  $T_{\text{co}}$  is for a given  $L_{\text{A,ph}}$ , so that the energy balance is satisfied between Poynting flux and heat conduction flux. The cooler  $T_{\text{co}}$  of the M dwarf results in lower plasma  $\beta$  for the stellar wind, in which the amplification of the Alfvén wave is promoted. The larger amplitude of the Alfvén wave is associated with the stronger slow shocks, which contribute to the faster stellar wind of the M dwarf. The faster  $v_{\text{wind}}$  and much smaller surface area of the M dwarf lead to a much smaller  $\dot{M}$  of the M dwarf’s wind.

By using the established semi-empirical method, we can predict the general trends of  $v_{\text{wind}}$ ,  $T_{\text{co}}$ , and  $\dot{M}$ , with respect to  $T_{\text{eff}}$  and  $L_{\text{A,ph}}$ , as illustrated in Figure 5 (see Appendix B). The open circles in this figure represent the samples of our parameter survey discussed in this Letter, about each of which several chromospheric magnetic field strengths are tested. The thick dashed line corresponds to the fiducial  $L_{\text{A,ph}}$  as a function of  $T_{\text{eff}}$ , which is calculated from the photospheric magnetic field, filling factor of open magnetic flux, and the velocity fluctuation of the convective motion. The thick dashed-dotted line corresponds to the largest  $L_{\text{A,ph}}$  obtained by assuming that the convective velocity reaches the sound speed on the photosphere. The thin dashed line represents  $L_{\text{A,ph}}$  as a function of  $T_{\text{eff}}$ , which results in  $v_{\text{wind}} = v_{\text{esc},*}$ . Along the thick dashed line, it is seen that stellar wind velocity ( $v_{\text{wind}}$ ) and coronal temperature ( $T_{\text{co}}$ ) are faster and cooler with decreasing  $T_{\text{eff}}$ , and that the mass-loss rate ( $\dot{M}$ ) of M dwarfs’ winds are much smaller than the solar wind’s value.

## 6. Discussion

Our wind’s mass-loss rates of M dwarfs are typically smaller than those reported by the previous global 3D stellar wind modelings using AWSOM. The  $\dot{M}$  of an M8 type star in this study is no more than  $6.9 \times 10^{-17} M_{\odot} \text{ yr}^{-1}$ , while Garraffo et al. (2017)

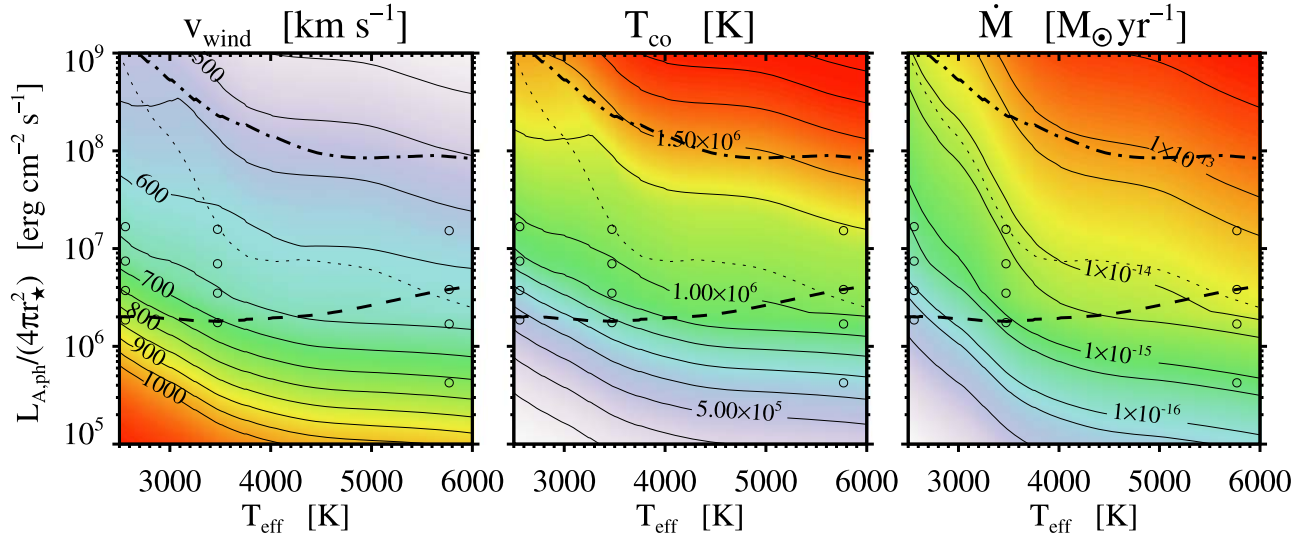


**Figure 5.** General trends of stellar wind velocity ( $v_{\text{wind}}$ ), coronal temperature ( $T_{\text{co}}$ ), and wind's mass-loss rate ( $\dot{M}$ ), with respect to the effective temperature ( $T_{\text{eff}}$ ) and Alfvén wave luminosity on the photosphere ( $L_{\text{A,ph}}$ ), which is predicted by our semi-empirical method. The open circles in this figure represent part of the samples in our parameter survey. The thick dashed line corresponds to the fiducial  $L_{\text{A,ph}}$  as a function of  $T_{\text{eff}}$ . The thick dashed-dotted line corresponds to the largest  $L_{\text{A,ph}}$  obtained by assuming that the convective velocity reaches the sound speed on the photosphere. The thin dashed line represents  $L_{\text{A,ph}}$  as a function of  $T_{\text{eff}}$ , which results in  $v_{\text{wind}} = v_{\text{esc}}$ .

and Dong et al. (2018) showed  $3 \times 10^{-14} M_{\odot} \text{yr}^{-1}$  and  $4.1 \times 10^{-15} M_{\odot} \text{yr}^{-1}$  for TRAPPIST-1 (M8), respectively. The  $\dot{M}$  of Proxima Centauri (M5.5) by Garraffo et al. (2016) and EV Lac (M3.5) by Cohen et al. (2014) are  $1.5 \times 10^{-14} M_{\odot} \text{yr}^{-1}$  and  $3 \times 10^{-14} M_{\odot} \text{yr}^{-1}$ , respectively, which are 10–100 times higher than reproduced in our simulation. These much larger mass-loss rates probably originate in their inner boundary conditions, corresponding to the top of the stellar chromosphere. In particular, our simulation does not validate their estimation of Alfvén wave energy injection, which is sometimes based on the widely used assumption of the constant “Poynting-flux-to-field ratio” (Sokolov et al. 2013). It is impossible for the above 3D modelings to reproduce our results because they are unable to consider the Alfvén wave dissipation and reflection from the stellar photosphere to the top of the chromosphere more self-consistently with the present computational resources.

Cranmer & Saar (2011) estimated that the  $\dot{M}$  of EV Lac (M3.5) is three orders of magnitude smaller than our simulation results for an M3.5 type star. This is because they assumed a much smaller Poynting flux on the photosphere compared to our simulation. The scaling law for  $\dot{M}$  proposed by Suzuki (2018) was also predicted to be 10–100 times smaller than our estimation. They performed numerical simulations that are similar to our study, but the low-mass stars with  $M_{\star} \geq 0.6 M_{\odot}$  are considered. According to their analysis, Alfvén wave transmissivity into the corona strongly depends on the stellar effective temperature ( $\propto T_{\text{eff}}^{13/2}$ ), which possibly leads to the underestimation of  $\dot{M}$  for cool dwarfs. Finally, we point out that the assumption of  $v_{\text{wind}} = v_{\text{esc}}$  used in both Cranmer & Saar (2011) and Suzuki (2018) misleadingly implies that  $\dot{M}$  depends on  $v_{\text{esc}}$ .

Observational measurements of an M dwarf's stellar wind are still very challenging. In order to quantify the stellar wind's properties observationally, Wood et al. (2005) investigated the absorption signatures in stellar Ly $\alpha$  spectra, leading to the estimation of  $\dot{M} \sim 2 \times 10^{-14} M_{\odot} \text{yr}^{-1}$  for EV Lac (M3.5). They also suggested an upper limit of Proxima Centauri's  $\dot{M} \sim 4 \times 10^{-15} M_{\odot} \text{yr}^{-1}$ . Bourrier et al. (2016) and Vidotto & Bourrier (2017) deduced  $\dot{M}$  of GJ 436 (M2.5) to be around

$(0.45\text{--}2.5) \times 10^{-15} M_{\odot} \text{yr}^{-1}$  by analyzing the transmission spectra of Ly $\alpha$  of GJ 436 b (a warm Neptune). While the observed  $\dot{M}$  of GJ 436 and the upper limit on  $\dot{M}$  of Proxima Centauri is not inconsistent with our results, the observed  $\dot{M}$  of EV Lac is much higher than the simulated value. Cranmer & Saar (2011) argued that the coronal mass ejection is possibly related to the observed high mass-loss rate of EV Lac. To clarify what causes the discrepancy between the observed and simulated  $\dot{M}$ , further self-consistent modeling is needed for the stellar wind and astrosphere.

T.S. was supported by JSPS KAKENHI grant No. JP18J12677. A part of this study was carried out by using the computational resources of the Center for Integrated Data Science, Institute for Space-Earth Environmental Research, Nagoya University through the joint research program, XC40 at YITP in Kyoto University, and Cray XC50 at Center for Computational Astrophysics, National Astronomical Observatory of Japan. Numerical analyses were partly carried out on analysis servers at the Center for Computational Astrophysics, National Astronomical Observatory of Japan.

## Appendix A Basic Equations

The basic equations in the axial symmetric magnetic flux tube are written as follows:

$$\frac{\partial \rho}{\partial t} + \frac{1}{A} \frac{\partial}{\partial x} (\rho v_x A) = 0, \quad (\text{A1})$$

$$\begin{aligned} & \frac{\partial}{\partial t} \left( \frac{p}{\gamma - 1} + \frac{1}{2} \rho v^2 + \frac{B^2}{8\pi} \right) \\ & + \frac{1}{A} \frac{\partial}{\partial x} \left[ A \left\{ \left( \frac{\gamma p}{\gamma - 1} + \frac{\rho v^2}{2} + \frac{B_{\phi}^2}{4\pi} \right) v_x - \frac{B_x}{4\pi} (B_{\phi} v_{\phi}) \right\} \right] \\ & = \rho v_x \frac{\partial}{\partial x} \left( \frac{GM_{\star}}{r} \right) - \frac{1}{A} \frac{\partial}{\partial x} (A F_c) - Q_{\text{rad}}, \end{aligned} \quad (\text{A2})$$

$$\frac{\partial(\rho v_x)}{\partial t} + \frac{\partial p}{\partial x} + \frac{1}{A} \frac{\partial}{\partial x} \left\{ \left( \rho v_x^2 + \frac{B_\phi^2}{8\pi} \right) A \right\} - \rho v_\phi^2 \frac{\partial \ln \sqrt{A}}{\partial x} - \rho \frac{\partial}{\partial x} \left( \frac{GM_\star}{r} \right) = 0, \quad (\text{A3})$$

$$\frac{\partial(\rho v_\phi)}{\partial t} + \frac{1}{A\sqrt{A}} \frac{\partial}{\partial x} \left\{ A\sqrt{A} \left( \rho v_x v_\phi - \frac{B_x B_\phi}{4\pi} \right) \right\} = 0, \quad (\text{A4})$$

$$\frac{\partial B_\phi}{\partial t} + \frac{1}{\sqrt{A}} \frac{\partial}{\partial x} (\sqrt{A} (v_x B_\phi - v_\phi B_x)) = 0, \quad (\text{A5})$$

$$\frac{dx}{dr} = \sqrt{1 + \left( \frac{d\sqrt{A}}{dr} \right)^2}. \quad (\text{A6})$$

Here,  $\gamma$  represents the specific heat ratio and is set to 5/3 in this study.  $F_c$  and  $Q_{\text{rad}}$  are the heat conduction flux and radiative cooling term, respectively.  $r$  is the distance from the center of the Sun.  $A$  is the cross section of the flux tube (i.e.,  $B_x A = \text{const.}$ ), and is related to  $r$  through the filling factor  $f$  as  $A(r) = 4\pi r^2 f(r)$ .  $f$  determines the geometry of the flux tube. The functions for  $F_c$ ,  $Q_{\text{rad}}$ , and  $f(r)$  are similar to those used in Sakaue & Shibata (2020).

## Appendix B

### Semi-empirical Method for Stellar Coronae and Winds

The derivation of our semi-empirical method is briefly summarized in this Appendix. More detailed discussion will appear in our subsequent paper (Sakaue & Shibata 2021, in preparation).

In Section 3, the stellar wind velocity ( $v_{\text{wind}}$ ) is determined according to the integral of equation of motion (Equation (1)).

$$v_{\text{wind}}^2 = \Delta_p + \Delta_{p_B} + \Delta_c + \Delta_t + \Delta_g, \quad (\text{B1})$$

where  $v_{\text{wind}}$  is the stellar wind velocity at  $r = 100r_\star$ , and  $\Delta_p = -2 \int_{r_\star}^{100r_\star} \left\langle \frac{1}{\rho} \frac{\partial p}{\partial x} \right\rangle dx$ ,  $\Delta_{p_B} = -2 \int_{r_\star}^{100r_\star} \left\langle \frac{1}{\rho} \frac{\partial}{\partial x} \left( \frac{B_\phi^2}{8\pi} \right) \right\rangle dx$ ,

$$\Delta_c = 2 \int_{r_\star}^{100r_\star} \left\langle v_\phi^2 \right\rangle \frac{\partial \ln \sqrt{A}}{\partial x} dx, \quad \Delta_t = -2 \int_{r_\star}^{100r_\star} \left\langle \frac{B_\phi^2}{4\pi\rho} \right\rangle \frac{\partial \ln \sqrt{A}}{\partial x} dx,$$

and  $\Delta_g = -v_{\text{esc}\star}^2 \left( 1 - \frac{1}{100} \right)$ . They are characterized by the maximum amplitude of Alfvén wave in the stellar wind ( $v_{\phi \text{max}}$ ) as follows:

$$\begin{aligned} \Delta_p + \Delta_g &= a_{1,1} \tilde{v}_{\phi \text{max}}^{k_{1,1}}, \quad \Delta_c = a_{1,2} \tilde{v}_{\phi \text{max}}^{k_{1,2}}, \\ \Delta_t &= -a_{1,3} \tilde{v}_{\phi \text{max}}^{k_{1,3}}, \quad \Delta_{p_B} = a_{1,4} |\tilde{\Delta}_c + \tilde{\Delta}_t|^{k_{1,4}}, \end{aligned} \quad (\text{B2})$$

where  $\tilde{v}_{\phi \text{max}} = v_{\phi \text{max}} / (300 \text{ km s}^{-1})$ ,  $\tilde{\Delta}_c = \Delta_c / (319^2 \text{ (km s}^{-1})^2)$ ,  $\tilde{\Delta}_t = \Delta_t / (319^2 \text{ (km s}^{-1})^2)$ . The coefficients ( $a_{1,1}$ ,  $a_{1,2}$ ,  $a_{1,3}$ ,  $a_{1,4}$ ) and power-law indices ( $k_{1,1}$ ,  $k_{1,2}$ ,  $k_{1,3}$ ,  $k_{1,4}$ ) are determined based on our simulation results

$$a_{1,1} = 653^2, \quad a_{1,2} = 585^2, \quad a_{1,3} = 666^2, \quad a_{1,4} = 472^2,$$

in unit of  $(\text{km s}^{-1})^2$ .

$$k_{1,1} = 2.31, \quad k_{1,2} = 2.04, \quad k_{1,3} = 2.12, \quad k_{1,4} = 0.682.$$

$v_{\phi \text{max}}$  is negatively correlated with the plasma  $\beta$  at the position where Alfvén wave amplitude reaches the maximum ( $\beta_{\phi \text{max}}$ ).

$$v_{\phi \text{max}} = a_2 \beta_{\phi \text{max}}^{-k_2}, \quad (\text{B3})$$

where  $a_2 = 286 \text{ km s}^{-1}$  and  $k_2 = 0.171$ .

$\beta_{\phi \text{max}}$  is determined by the coronal temperature  $T_{\text{co}}$  and  $v_{\text{wind}}$ .

$$\beta_{\phi \text{max}} = a_3 \left( \frac{\tilde{T}_{\text{co}}}{\tilde{v}_{\text{wind}}} \right)^{k_3}, \quad (\text{B4})$$

where  $\tilde{T}_{\text{co}} = T_{\text{co}} / (10^6 \text{ K})$ ,  $\tilde{v}_{\text{wind}} = v_{\text{wind}} / (600 \text{ km s}^{-1})$ ,  $a_3 = 2.09 \times 10^{-2}$  and  $k_3 = 1.85$ .

The coronal temperature ( $T_{\text{co}}$ ) is determined by the balance between heat conduction flux and the transmitted Poynting flux into the corona, according to the energy conservation law (Equation (3)). This is similar to the analytical models of quiescent and flaring coronal loops (Rosner et al. 1978; Yokoyama & Shibata 1998). Hereafter, we discuss the following equation, which is obtained by dividing the both sides of Equation (3) with  $L_{A,\text{co}}$ .

$$\alpha_{c/A} = 1 - \alpha_{\text{wind}/A} (1 + v_{\text{esc}\star}^2 / v_{\text{wind}}^2), \quad (\text{B5})$$

where  $\alpha_{c/A}$  and  $\alpha_{\text{wind}/A}$  represent the energy conversion efficiency from  $L_{A,\text{co}}$  to  $L_{c,\text{co}}$  and  $L_{\text{kin},\text{wind}}$  (i.e.,  $L_{c,\text{co}} = -\alpha_{c/A} L_{A,\text{co}}$  and  $L_{\text{kin},\text{wind}} = \alpha_{\text{wind}/A} L_{A,\text{co}}$ ). Note that when  $v_{\text{wind}} < v_{\text{esc}\star}$ ,  $\alpha_{c/A}$  is often quenched to zero, which means that the approximation for Equations (3) and (B5) become invalid. To avoid this problem, we assumed the monotonic increase in  $L_{c,\text{co}}$  with  $L_{A,\text{co}}$  i.e.,  $\partial \ln \alpha_{c/A} / \partial \ln L_{A,\text{co}} > -1$ .

We also confirmed that the coefficient  $\alpha_{\text{wind}/A}$  is almost invariant in our parameter survey about the stars, chromospheric magnetic field strengths, and energy inputs from the photosphere, namely  $\alpha_{\text{wind}/A} = 0.442 \pm 0.166$ . Therefore,  $\alpha_{\text{wind}/A}$  is assumed to be constant in this study. It should be noted that, however,  $\alpha_{\text{wind}/A}$  possibly depends on the filling factor of open flux tube ( $f_{\text{ph}}$ ), which is beyond our present parameter survey.

By defining the spatial scale of expanding magnetic flux tube ( $l_B$ ) as below, the coronal temperature ( $T_{\text{co}}$ ) is estimated as Equation (B7).

$$l_B = \int_1^{\bar{B}/B_{x,\text{co}}} \left| \frac{d \ln B_x}{dx} \right|^{-1} d \left( \frac{B_x}{B_{x,\text{co}}} \right) \quad (\text{B6})$$

$$T_{\text{co}} = a_4 \left[ \left\{ 1 - \alpha_{\text{wind}/A} \left( 1 + \frac{v_{\text{esc}\star}^2}{v_{\text{wind}}^2} \right) \right\} \tilde{F}_{A,\text{co}} \tilde{l}_B \right]^{k_4}, \quad (\text{B7})$$

where  $\bar{B}$  and  $B_{x,\text{co}}$  are the magnetic field strengths in the chromosphere and corona.  $\tilde{F}_{A,\text{co}} = F_{A,\text{co}} / (10^5 \text{ erg cm}^{-2} \text{ s}^{-1})$ ,  $\tilde{l}_B = l_B / r_\odot$ .  $a_4 = 1.62 \times 10^6 \text{ K}$ ,  $k_4 = 0.256$ . Note that  $l_B$  is determined only by the assumed geometry of magnetic flux tube.

Finally,  $L_{A,\text{co}}$  should be expressed as a product of  $L_{A,\text{ph}}$  which is the Alfvén wave luminosity on the stellar photosphere and the transmissivity of Alfvén wave from the photosphere to corona ( $\alpha_{\text{co/ph}}$ , i.e.,  $L_{A,\text{co}} = \alpha_{\text{co/ph}} L_{A,\text{ph}}$ ). The dissipation and reflection of Alfvén wave in the stellar chromosphere could reduce  $\alpha_{\text{co/ph}}$ .

$\alpha_{\text{co/ph}}$  is well described by the Alfvén travel time from the photosphere to the corona ( $\tau_{A,\text{co}}$ ), especially the normalized

one by the typical wave frequency of Alfvén wave ( $\nu_A$ ). We interpreted  $\nu_A$  with the acoustic cutoff frequency of stellar photosphere ( $\nu_{ac}$ ), and found the following:

$$\alpha_{co/ph} = a_{5,1}(\tau_{A,co}\nu_{ac}/a_{5,2})^{k_5}, \quad (B8)$$

where  $a_{5,1} = 2.41 \times 10^{-2}$  and  $a_{5,2} = 1.04$ .  $k_5 = 1.25$  when  $\tau_{A,co}\nu_{ac} < 1.04$ , and otherwise,  $k_5 = -1.10$ .  $\tau_{A,co}\nu_{ac}$  is empirically expressed as a function of  $g_*$ , chromospheric magnetic field strength ( $\bar{B}$ ), and velocity amplitude on the photosphere ( $v_{ph}$ ):

$$\tau_{A,co}\nu_{ac} = a_6 \tilde{g}_*^{k_{6,1}} \left( \frac{\bar{B}}{B_{ph}} \right)^{-k_{6,2}} \left( \frac{v_{ph}}{c_{s,ph}} \right)^{k_{6,3}}, \quad (B9)$$

where  $c_{s,ph}$  and  $B_{ph}$  are the adiabatic sound speed and magnetic field strength on the photosphere.  $a_6 = 0.921$ ,  $k_{6,1} = 0.240$ ,  $k_{6,2} = 0.408$ , and  $k_{6,3} = 0.697$ .

Based on Equations (B6)–(B9),  $T_{co}$  is obtained as a function of  $v_{wind}$  and  $L_{A,ph}$  (or  $v_{ph}$ ) by specifying the basic parameters ( $g_*$ ,  $B_{ph}$ ,  $\bar{B}$ ,  $c_{s,ph}$ ,  $v_{esc,*}$ ,  $\alpha_{wind/A}$ ,  $l_B$ ). These parameters can be related to the stellar effective temperature  $T_{eff}$  by limiting our discussion to the main-sequence stars' atmospheres and winds. On the other hand, Equations (B1)–(B4) show that  $v_{wind}$  should be determined implicitly when  $T_{co}$  is given. By using some iterative method, therefore,  $T_{co}$  and  $v_{wind}$  are calculated for given  $L_{A,ph}$  and  $T_{eff}$ . From the obtained  $v_{wind}$  and the definition of  $L_{kin,wind}$ , the mass-loss rate of stellar wind ( $\dot{M}$ ) is expressed as follows:

$$\dot{M} = 2\alpha_{wind/A} \alpha_{co/ph} \frac{L_{A,ph}}{v_{wind}^2} \quad (B10)$$

Sakaue & Shibata (2021, in preparation) will explain the derivation of the above coefficients ( $a_{1,1}$ ,  $a_{1,2}$ ,  $a_{1,3}$ ,  $a_{1,4}$ ,  $a_2$ ,  $a_3$ ,  $a_4$ ,  $a_{5,1}$ ,  $a_{5,2}$ ,  $a_6$ ) and power-law indices ( $k_{1,1}$ ,  $k_{1,2}$ ,  $k_{1,3}$ ,  $k_{1,4}$ ,  $k_2$ ,  $k_3$ ,  $k_4$ ,  $k_5$ ,  $k_{6,1}$ ,  $k_{6,2}$ ,  $k_{6,3}$ ) with more simulation results for some M dwarfs (M0, M5, M5.5).

## ORCID iDs

Takahito Sakaue  <https://orcid.org/0000-0002-3427-4590>

## References

- Alvarado-Gómez, J. D., Drake, J. J., Fraschetti, F., et al. 2020, *ApJ*, **895**, 47  
 Bourrier, V., Lecavelier des Etangs, A., Ehrenreich, D., et al. 2016, *A&A*, **591**, A121  
 Cohen, O., Drake, J. J., Gloer, A., et al. 2014, *ApJ*, **790**, 57  
 Cranmer, S. R., & Saar, S. H. 2011, *ApJ*, **741**, 54  
 Dong, C., Jin, M., Lingam, M., et al. 2018, *PNAS*, **115**, 260  
 Freedman, R. S., Lustig-Yaeger, J., Fortney, J. J., et al. 2014, *ApJS*, **214**, 25  
 Garraffo, C., Drake, J. J., & Cohen, O. 2016, *ApJL*, **833**, L4  
 Garraffo, C., Drake, J. J., Cohen, O., Alvarado-Gómez, J. D., & Moschou, S. P. 2017, *ApJL*, **843**, L33  
 Gillon, M., Jehin, E., Lederer, S. M., et al. 2016, *Natur*, **533**, 221  
 Hollweg, J. V., Jackson, S., & Galloway, D. 1982, *SoPh*, **75**, 35  
 Khodachenko, M. L., Ribas, I., Lammer, H., et al. 2007, *AsBio*, **7**, 167  
 Kudoh, T., & Shibata, K. 1999, *ApJ*, **514**, 493  
 Lammer, H., Lichtenegger, H. I. M., Kulikov, Y. N., et al. 2007, *AsBio*, **7**, 185  
 Linsky, J. 2019, *Lecture Notes in Physics* (Berlin: Springer)  
 Ludwig, H.-G., Allard, F., & Hauschildt, P. H. 2002, *A&A*, **395**, 99  
 Ludwig, H.-G., Freytag, B., & Steffen, M. 1999, *A&A*, **346**, 111  
 Magic, Z., Weiss, A., & Asplund, M. 2015, *A&A*, **573**, A89  
 Maldonado, J., Affer, L., Micela, G., et al. 2015, *A&A*, **577**, A132  
 Matsumoto, T. 2021, *MNRAS*, **500**, 4779  
 Matsumoto, T., & Shibata, K. 2010, *ApJ*, **710**, 1857  
 Matsumoto, T., & Suzuki, T. K. 2012, *ApJ*, **749**, 8  
 Matsumoto, T., & Suzuki, T. K. 2014, *MNRAS*, **440**, 971  
 Mesquita, A. L., & Vidotto, A. A. 2020, *MNRAS*, **494**, 1297  
 Meyer, C. D., Balsara, D. S., & Aslam, T. D. 2012, *MNRAS*, **422**, 2102  
 Miyoshi, T., & Kusano, K. 2005, *JCoPh*, **208**, 315  
 Rosner, R., Tucker, W. H., & Vaiana, G. S. 1978, *ApJ*, **220**, 643  
 Sakaue, T., & Shibata, K. 2020, *ApJ*, **900**, 120  
 Scalo, J., Kaltenegger, L., Segura, A. G., et al. 2007, *AsBio*, **7**, 85  
 Seager, S. 2013, *Sci*, **340**, 577  
 Shoda, M., Suzuki, T. K., Asgari-Targhi, M., et al. 2019, *ApJL*, **880**, L2  
 Shoda, M., Suzuki, T. K., Matt, S. P., et al. 2020, *ApJ*, **896**, 123  
 Shoda, M., Yokoyama, T., & Suzuki, T. K. 2018, *ApJ*, **853**, 190  
 Shu, C.-W., & Osher, S. 1988, *JCoPh*, **77**, 439  
 Sokolov, I. V., van der Holst, B., Oran, R., et al. 2013, *ApJ*, **764**, 23  
 Suzuki, T. K. 2018, *PASJ*, **70**, 34  
 Suzuki, T. K., Imada, S., Kataoka, R., et al. 2013, *PASJ*, **65**, 98  
 Suzuki, T. K., & Inutsuka, S.-i. 2005, *ApJL*, **632**, L49  
 Suzuki, T. K., & Inutsuka, S.-i. 2006, *JGRA*, **111**, A06101  
 Tarter, J. C., Backus, P. R., Mancinelli, R. L., et al. 2007, *AsBio*, **7**, 30  
 van der Holst, B., Sokolov, I. V., Meng, X., et al. 2014, *ApJ*, **782**, 81  
 Velli, M. 1993, *A&A*, **270**, 304  
 Vidotto, A. A., & Bourrier, V. 2017, *MNRAS*, **470**, 4026  
 Vidotto, A. A., Jardine, M., Morin, J., et al. 2014, *MNRAS*, **438**, 1162  
 Wood, B. E., Müller, H.-R., Zank, G. P., Linsky, J. L., & Redfield, S. 2005, *ApJL*, **628**, L143  
 Yokoyama, T., & Shibata, K. 1998, *ApJL*, **494**, L113